Eur. Phys. J. A **6**, 329–344 (1999)

THE EUROPEAN PHYSICAL JOURNAL A

Determination of the neutron electric form factor from the reaction $^3\mathrm{He}(\mathrm{e}, e'n)$ at medium momentum transfer

J. Becker[1a], H.G. Andresen[2], J.R.M. Annand[3], K. Aulenbacher[2], K. Beuchel[1], J. Blume–Werry[2], Th. Dombo[2], P. Drescher[1], M. Ebert[1], D. Eyl[2], A. Frey[2], P. Grabmayr[4], T. Großmann[1], P. Hartmann[1], T. Hehl[4], W. Heil[1], C. Herberg[2], J. Hoffmann[1], J.D. Kellie[3], F. Klein[5], K. Livingston[3], M. Leduc[6], M. Meyerhoff[1], H. Möller[2], Ch. Nachtigall[1], A. Natter[4], M. Ostrick[2], E.W. Otten[1], R.O. Owens[3], S. Plützer[1], E. Reichert[1], D. Rohe[1], M. Schäfer[1], H. Schmieden[2], R. Sprengard[2], M. Steigerwald[1], K.–H. Steffens[2], R. Surkau[1], Th. Walcher[2], R. Watson[3], E. Wilms[1]

[1] Institut für Physik, Universität Mainz, 55099 Mainz, Germany
[2] Institut für Kernphysik, Universität Mainz, 55099 Mainz, Germany
[3] Department of Physics and Astronomy, University of Glasgow, Glasgow, UK
[4] Physikalisches Institut, Universität Tübingen, 72076 Tübingen, Germany
[5] Physikalisches Institut, Universität Bonn, 53115 Bonn, Germany
[6] École Normale Superiéure, Paris, France

Received: 29 April 1999
Communicated by B. Povh

Abstract. The electric form factor of the neutron G_{En} has been determined in double polarized exclusive $^3\mathbf{He}(\mathbf{e}, e'n)$ scattering in quasi–elastic kinematics by measuring asymmetries $A_\perp, A_\parallel$ of the cross section with respect to helicity reversal of the electron, with the nuclear spin being oriented perpendicular to the momentum transfer $\mathbf{q}$ in case of $A_\perp$ and parallel in case of $A_\parallel$. The experiment was performed at the 855 MeV c. w. microtron MAMI at Mainz. The degree of polarization of the electron beam and of the gaseous $^3\mathbf{He}$ target were each about 50 %. Scattered electrons and neutrons were detected in coincidence by detector arrays covering large solid angles. Quasi–elastic scattering events were reconstructed from the measured electron scattering angles ϑ_e, φ_e and the neutron momentum vector $\mathbf{p}'_n$ in the plane wave impulse approximation. We obtain the result $\langle G_{En} \rangle_{\,(0.27 \le \mathrm{Q^2c^2/GeV^2} \le 0.5)} = 0.0334 \pm 0.0033_{\mathrm{stat}} \pm 0.0028_{\mathrm{syst}}$ which is averaged over the indicated range of Q^2, the squared momentum transfer. This G_{En} value is significantly smaller than measured from the $D(\mathbf{e}, e'\mathbf{n})$ reaction under similar kinematical conditions. To what extent final state interactions in ^{3}He quench the G_{En} result is subject of calculations currently in progress elsewhere.

PACS. 14.20.Dh Properties of specific particles: Protons and neutrons – 24.70.+s Nuclear reactions: Polarization phenomena in reactions – 13.40.Gp Specific reactions and phenomenology: Electromagnetic form factors – 25.10.+s Nuclear reactions involving few–nucleon systems – 25.30.Fj Nuclear reactions: Inelastic electron scattering to continuum

1 Introduction

The investigation of the nucleon structure is a major focus of contemporary hadron physics. Experimentally this may be ach-ieved by scattering high energy leptons from nucleons to reveal their electromagnetic structure. This is characterized by two sets of functions, the form factors for the elastic scattering channel and the so-called structure functions for the deep inelastic one. Roughly speaking the former represents the spatial distribution of the partons within a nucleon, the latter their momentum distribution. Form factors and structure functions are cornerstones on which to test any theoretical nucleon model [1].

Form factors are functions of the square of the momentum transfer in the scattering process

$$Q^2 = -q^\mu q_\mu \tag{1}$$

with q^μ being the four momentum transfer. Elastic electron scattering from nucleons can be described by the two Sachs form factors [2] G_E and G_M. In the Breit frame, which is characterized by $Q^2 = \mathbf{q}^2$ (no energy transfer), they can be interpreted as Fourier transforms of the distributions of charge and magnetism, respectively. Thus they are normalized at the point $Q = 0$ to the values of the

[a] comprises part of Ph.D. thesis; e-mail: becker@kph.uni-mainz.de

total charge and the magnetic moment, respectively. Precise G_{Ep} and G_{Mp} values have been extracted for the proton from scattering cross sections measured at momentum tranfers of up to $Q^2 = 5$ (GeV/c)^2 and $Q^2 = 20$ (GeV/c)^2, respectively [3,4]. Due to their comparable size the electric and magnetic contribution can be separateded by the well–known technique of Rosenbluth separation. G_{Mp} follows, within a 10 % margin, the empirical dipole form:

$$\frac{G_{Mp}}{\mu_p} \approx G_D = \left(1 + \frac{Q^2}{0.71(GeV/c)^2}\right)^{-2}. \qquad (2)$$

For the case of the neutron, however, the electric contribution to the cross section never exceeds the 5 % level over the entire Q^2 range due to the zero integral charge. For this reason our knowledge of G_{En} is still rather poor whereas G_{Mn}, which also follows closely the dipole form (2), is known much better. Scattering off neutrons can be studied in general only for neutrons bound in nuclei and G_{En} obtained thus must be corrected for nuclear effects such as final state interactions (FSI), mesonic exchange currents (MEC) and possibly also nuclear medium effects on G_{En} itself. They may have stronger impact on the tiny G_{En} than on the robust G_{Mn}. The latter has been measured recently by several groups [5–9] in the range $Q^2 < 1$ (GeV/c)^2 similar to that covered in the present experiment. They have performed simultaneous measurements of quasi–elastic neutron and proton scattering from a deuterium target and extracted G_{Mn} from the ratio of cross sections:

$$R_{n/p} = \frac{\sigma(D(e, e'n))}{\sigma(D(e, e'p))}. \qquad (3)$$

This ratio is independent of the spectral functions of proton and neutron in this self–conjugate nucleus in leading order. Although two of these measurements [6,7] claim statistical precisions on the 1 % and 3 % levels, respectively, at $0.27 \leq \mathrm{Q^2c^2/GeV^2} \leq 0.5$ their results for G_{Mn} differ in this range by about 12 %. At present this discrepancy is under discussion [10,11]. For the present analysis of G_{En}, which uses G_{Mn} as an input parameter (see Sect. 2), we rely on the dipole fit to G_{Mn}. It agrees well with the result of [6]. We account for the unresolved discrepancy in G_{Mn} by assuming a systematic error of 5 % (see Table 3, row 11):

$$G_{Mn}/(\mu_n G_D) = 1.00 \pm 0.05. \qquad (4)$$

The present knowledge of G_{En} is summarized as follows: The mean squared charge radius of the neutron $\langle r^2 \rangle_{ch}$ has been determined in the limit $Q^2 \to 0$ by scattering thermal and epithermal neutrons from heavy diamagnetic atoms with even-even nuclei, such as xenon or lead. The elastic scattering amplitude from the atomic electrons is proportional to G_{En}. The most recent result has determined the slope of G_{En} at the origin from the neutron transmission of liquid thorogenic ^{208}Pb as [12]

$$\left.\frac{dG_{En}}{dQ^2}\right|_{Q^2=0} = 0.492 \pm 0.012 \pm 0.013 \ (GeV/c)^{-2}. \qquad (5)$$

At high momentum transfer, $Q^2 = 1.75 - 4$ (GeV/c)^2, quasi–elastic e–D scattering results [13] have given values of G_{En} consistent with zero and G_{Mn} consistent with the dipole form. These results are at odds with the theoretical prediction $G_{En} = -\tau G_{Mn}$ [13] with $\tau = Q^2/(4M^2)$ and M being the neutron mass.

At medium momentum transfer, $0.2 \leq Q^2c^2/GeV^2 \leq 0.7$, where the photon resolution is of the order of the nucleon size, G_{En} is significantly greater than zero. The present knowledge of G_{En} in this range stems from measurements that exploit interference effects between the small form factor G_{En} and some other larger form factor. Through these effects the contribution of G_{En} to the signal is enhanced, as compared to a conventional Rosenbluth separation. One such experiment is elastic electron scattering from deuterium, where the electron is scattered coherently from the proton and the neutron and consequently the cross section has a contribution $\sim G_{En} \cdot G_{Ep}$. The major problem of the analysis is in separating the contributions of the proton and neutron due to uncertainties in the deuteron wave function [14,15].

Another approach to G_{En} via an interference term is the measurement of asymmetries in double polarized, exclusive, quasi–elastic scattering of electrons from neutrons in light nuclei like D or ^{3}He. The nucleon may be polarized either in the initial state, as in $^3\mathbf{He}(\mathbf{e}, e'n)$, or the polarization of the outgoing nucleon may be measured, as in $D(\mathbf{e}, e'\mathbf{n})$. Such exclusive coincidence experiments are performed preferably at 100 % duty cycle accelerators such as MAMI, because of the improvements in signal to background ratio with respect to earlier attempts with pulsed beams [16–18].

The A3–Collaboration at MAMI has performed measurements of G_{En} through the reactions $^3\mathbf{He}(\mathbf{e}, e'n)$ and $D(\mathbf{e}, e'\mathbf{n})$ employing one common detector setup. Eventually the comparison of the respective G_{En} values may allow in addition to search for a possible modification of the neutron structure inside these very different nuclei.

Apart from this still speculative effect (compare e.g. [19–21]) more conventinal nuclear structure effects, stemming from the wave function, final state interaction (FSI) and meson exchange currents (MEC) cause corrections. For the rather high Q^2 range of $0.27 \leq Q^2c^2/\mathrm{GeV^2} \leq 0.5$ of this experiment, the FSI and MEC corrections were expected to be small on the basis of the calculations of [22, 23] and experimental evidence from analogue nuclear reaction experiments like $^3\mathbf{He}(\mathbf{p}, p'n \text{ or } 2p)$ [24,25]. However, the $^3\mathbf{He}(e, e'n)$ experiment at NIKHEF, which was sensitive to FSI effects through the transverse target asymmetry $A_Y^0(Q^2)$, does not support this assumption [26]. In relation to the small observable, namely the G_{En} amplitude in the interference term, even a minute admixture of FSI and other nuclear effects will have a large impact, requiring quantitative calculations for a safe interpretation. A dedicated Faddeev calculation, which covers exactly the kinematical range of our experiment, is underway at Bochum [27] in an attempt to quantitfy these effects in $^3\mathbf{He}(\mathbf{e}, e'n)$.

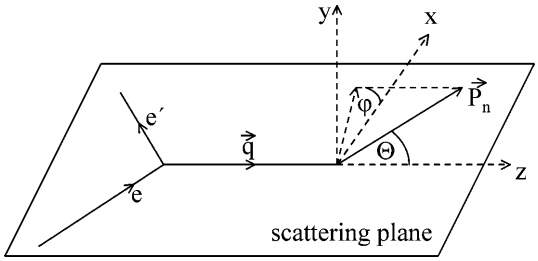

Fig. 1. Definition of the angle Θ between the neutron polarization $\mathbf{P}_n$ in the scattering plane and the momentum transfer vector $\mathbf{q}$ and of the out–of–plane angle φ. For $\varphi = 0^o$ and 180^o, respectively, $\mathbf{P}_n$ is aligned in the scattering plane. Asymmetries at $\Theta = 90^o$, $\varphi = 0^o$ and at $\Theta = 0^o$ are referred to as A_I and A_S, respectively

A pilot study of $^3\mathbf{He}(\mathbf{e}, e'n)$ [28], which used a subset of the present electron and neutron detection system, produced a value $G_{En}(Q^2 = 0.31\ \mathrm{GeV}^2/c^2) = 0.035 \pm 0.012 \pm 0.005$.

2 Concept of the double polarization experiment

The $^3\mathbf{He}(\mathbf{e}, e'n)$ reaction in quasi–elastic kinematics approximates to the scattering of a polarized electron from a polarized free neutron as the two protons in ^{3}He are dominantly (≈ 90 % of the wave function) in a spin–zero S–state and the neutron carries most of the ^{3}He spin [24,29, 30]. The double polarization measurement yields an asymmetry in the cross section, with respect to helicity reversal of the incoming electron, due to the following effects: In transverse geometry the cross section is composed coherently of electric and magnetic scattering amplitudes f and g, respectively. Transverse geometry is characterised by an angle $\Theta = 90^o$ between the momentum transfer vector $\mathbf{q}$ and the neutron spin and by an out–of–plane angle φ of 0^o or 180^o, corresponding to spin alignment in the scattering plane (see Fig. 1). In this geometry the magnetic dipole–dipole amplitude g just changes sign with respect to helicity reversal whereas the electric Coulomb amplitude f remains unchanged. Hence the cross sections for helicity states "+" and "-"

$$\sigma^{\pm} \sim |f \pm g|^2 = |f|^2 \pm 2\,\Re(f^* g) + |g|^2 \qquad (6)$$

exhibit an interference term obtainable from the asymmetry

$$A_I = \frac{\sigma^+ - \sigma^-}{\sigma^+ + \sigma^-} = \frac{2\,\Re(f^* g)}{|f|^2 + |g|^2}. \qquad (7)$$

In the asymmetry A_I the small effect of Coulomb scattering from the neutron is enhanced by the large magnetic one. Furthermore, many sources of systematic errors, such as uncertainties in luminosity and detection efficiency, drop out in an asymmetry measurement by taking ratios of cross sections. In parallel geometry, $\Theta = 0^o$, the asymmetry A_S with respect to helicity reversal projects out the helicity dependence of the spin–flip part of the cross section. It is of purely magnetic origin.

The total asymmetry for scattering of longitudinally polarized electrons from polarized free neutrons at rest, oriented at any angles Θ, φ, is given by [31,32]

$$\begin{aligned} A &= P_e P_n V \frac{a\, sin\Theta\, cos\varphi\, G_{En} G_{Mn} + b\, cos\Theta\, G_{Mn}^2}{c\, G_{En}^2 + d\, G_{Mn}^2} \qquad (8) \\ &= A_I\, sin\Theta\, cos\varphi + A_S\, cos\Theta. \end{aligned}$$

The coefficients $a...d$ are kinematic variables.

$$a = -2\sqrt{\tau(1+\tau)}\, tan(\vartheta_e/2) \qquad (9)$$

$$b = -2\tau\sqrt{1 + \tau + (1+\tau)^2\, tan^2(\vartheta_e/2)}\, tan(\vartheta_e/2) \qquad (10)$$

$$c = 1 \qquad (11)$$

$$d = \tau + 2\tau(1+\tau) tan^2(\vartheta_e/2) \qquad (12)$$

They depend on the electron scattering angle in the laboratory frame ϑ_e and on τ. At a given beam energy E, Q^2 and hence τ may be expressed in terms of ϑ_e

$$Q^2 = \frac{4E^2 sin^2(\vartheta_e/2)}{1 + \frac{2E}{M} sin^2(\vartheta_e/2)}. \qquad (13)$$

P_e and P_n are the degrees of polarization of the electron and neutron, respectively. The dilution factor

$$V = S/(S+B) \qquad (14)$$

is calculated from the unpolarized background B and the true signal S. To cover the more general case of a neutron in motion with initial momentum $\mathbf{p}_n$ a Lorentz transformation into the rest frame of the neutron has to be performed which introduces a dependence of the kinematical factors in (8) on $\mathbf{p}_n$ (compare Sect. 5.5 and App. A).

As seen from the kinematical coefficients a to d, A_S approaches 1 for backward scattering ($\vartheta_e = 180^o$) in the ideal case of fully polarized scattering ($P_e P_n = 1$) and $V = 1$. This is due to the vanishing of the spin–flip cross section for aligned spins $\mathbf{P}_e \mathbf{P}_n = +1$, independent of any form factor. Moreover, in the approximation $G_{En}^2 \ll G_{Mn}^2$ the form factors in A_S cancel at any kinematics resulting in

$$A_S = P_e P_n V (b/d). \qquad (15)$$

Around $\Theta = 90^o$ where the G_{En} dependent part of the asymmetry is maximal the total A is also very sensitive to Θ as illustrated in Fig. 2. The curves were calculated according to (8) assuming a free neutron at rest, $P_e = P_n = V = 1$, $G_{Mn} = \mu_n G_D$ (dipole form factor) and a parametrization for G_{En} suggested by Galster [15]

$$G_{En} = \frac{-\tau}{1 + \eta\tau} G_{Mn} \qquad (16)$$

with η as free parameter. Large η values correspond to small G_{En}. The kinematical constants (9)–(12) were calculated for E = 855 MeV and $\vartheta_e = 46^o$. One can see that for any realistic choice (η larger than about 3) A_I is much smaller than A_S which causes the strong dependence of

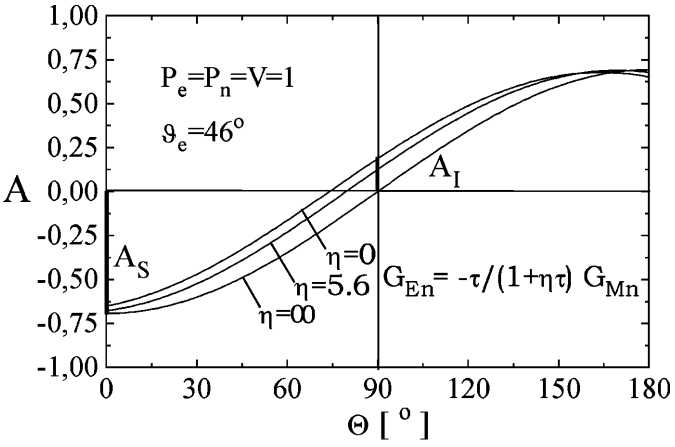

Fig. 2. Asymmetry A of elastic $\mathbf{n}(\mathbf{e}, e')$ scattering as function of the angle Θ between neutron polarization $\mathbf{P}_n$ and momentum transfer $\mathbf{q}$ for $\varphi = 0^o$ and different values η of the Galster parametrization (16) of G_{En}

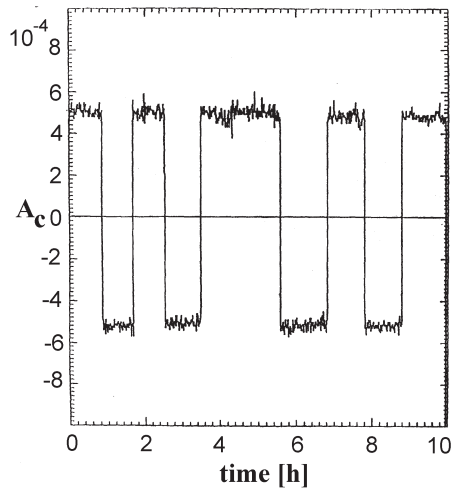

Fig. 3. Compton asymmetry A_c accumulated over a period of 10 h by measuring the γ–helicity dependent transmission through a magnetized iron absorber using two ionization chambers. The change in sign results from reversal of the iron magnetization

A on Θ around $\Theta = 90^o$ and hence requires a precise knowledge of the latter in order to determine A_I reliably (see Sect. 5). In the present experiment A was measured in both perpendicular and parallel geometry. The experimental analysis then reduces to a determination of the ratio

$$\frac{A_{I,ex}}{A_{S,ex}} = \frac{a}{b}\frac{G_{En}}{G_{Mn}} \tag{17}$$

in which the factor $P_e P_n V$ drops out. The kinematical factors a and b vary significantly over the range of electron detector acceptance $39^o \leq \vartheta_e \leq 59^o$ for both spin settings. This circumstance as well as the critical dependence on Θ require a kinematical reconstruction of each event. G_{En} is extracted from (17) with G_{Mn} set to the dipole value as defined by (2). As a cross check the measured value $A_{S,ex}$ will be compared to the one calculated from (15).

Within the framework of this paper G_{En} has been analyzed and discussed in terms of the plane wave impulse approximation (PWIA).

3 Experimental setup

3.1 Electron beam

The experiment was carried out at the 855 MeV c. w. electron accelerator MAMI with an average beam current of $\langle i \rangle = 7$ μA at the target. Circularly polarized laser light incident on a strained GaAsP crystal produced ≈ 50 % polarized electrons [33,34]. A spin rotator [35] between the polarized e^-–source and the first acceleration stage was used to align the e^-–polarization to be longitudinal at the target position. The electron helicity was switched randomly every second by a Pockels cell. P_e was measured off–line before and after each data taking period by Mott polarimetry [36,35] to a relative accuracy of 5 % [37]. During data taking, P_e was monitored continuously by a Compton polarimeter [38,39] incorporated in the beam dump. The analyzing power of the Compton polarimeter was $\approx 10^{-3}$ consistent with the calculated value [40]. Figure 3 shows the measured Compton asymmetry A_c over a 10 h period during the experiment.

3.2 The detector system

Large–solid–angle electron and neutron detectors were used to obtain the desired statistical accuracies in a reasonable measuring time (see Fig. 4). Both systems had sufficient granularity to allow for an adequate event–by–event kinematic reconstruction.

Electrons were detected in a calorimeter of 256 closely pa-cked lead glass Čerenkov counters, each with a frontal area of (4 x 4) cm^2 and a length of 29 cm (11 radiation lengths) [41]. The electromagnetic shower produced by a ≈ 700 MeV electron extends on average to 10 neighbouring modules. The sum signal provides an energy resolution $\Delta E_{e'}/E_{e'}$ of 20 % FWHM and cluster analysis provides a lateral spatial resolution of 10 mm standard deviation. The former is sufficient to separate the quasi–elastic peak from other, strongly inelastic processes such as π–production and excitation of nucleon resonances (see Fig. 8), but is inadequate for reconstruction of the $\mathbf{q}$–vector. At a distance of 1.85 m from the target the lateral resolution, on the other hand, yields a precise measurement of the electron scattering angles ϑ_e and φ_e, with a σ of 0.7^o and 0.3^o respectively. The former is mainly determined by the position uncertainty of the scattering vertex in the target cell (see Sect. 4.1). The whole calorimeter covers a solid angle of 100 msr at angles $39^o \leq \vartheta_e \leq 59^o$ and $-13^o \leq \varphi_e \leq 13^o$. The lead glass matrix runs in coincidence with a focussing air Čerenkov detector that suppresses background from electrons scattered in the entrance or exit windows of either the target cell or the beam

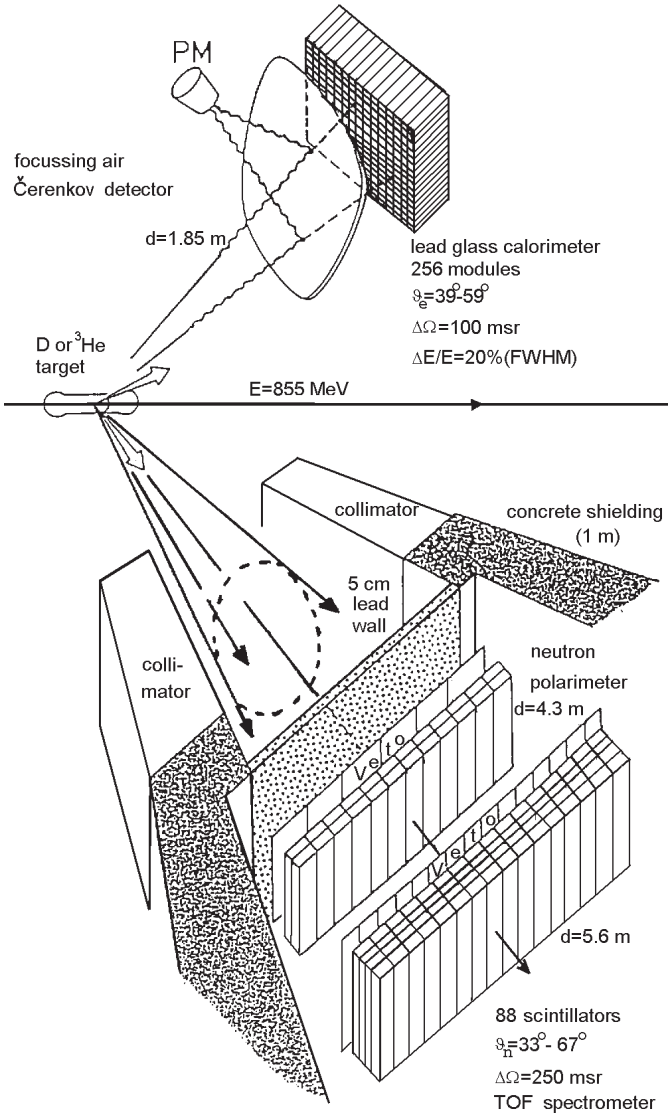

Fig. 4. Detector setup

line and also high energy photons resulting from π^o production.

The neutron detector array [42,43] covers a solid angle of 250 msr ($33^o \leq \vartheta_n \leq 67^o$ and $-20^o \leq \varphi_n \leq 20^o$) and thus accepts almost the entire Fermi distribution of quasi–elastic neutrons. It consists of 2 walls of plastic scintillator positioned at respective average distances of 4.3 m and 5.6 m from the target. This separation also allows neutron polarization measurement by double scattering, which is required for the $D(\mathbf{e}, e'\mathbf{n})$ experiment running in parallel with this one with the same detector setup [44,45]. In the present case only a single neutron hit in either of the walls was required. The 24 bars in the front wall (2 sublayers of 12 bars, each) had dimensions 180 cm long · 20 cm wide · 10 cm thick and the 64 in the rear wall (4 sublayers of 16 bars, each) were $300 \cdot 20 \cdot 5$ cm^3. The width determines the polar angle uncertainty $\Delta\vartheta_n$ to be 1.3^o for the front wall and 1.0^o for the rear wall.

Scintillation light is detected at both ends of each bar by photomultipliers. For each signal the time walk due to leading edge timing was corrected by an algorithm described in [43] using the pulse height information. The time difference between the two signals defines the vertical hit position with a σ of 5 cm, corresponding to an azimuthal resolution of $\Delta\varphi_n = 0.7^o$ for the front wall and 0.5^o for the rear wall. The mean time of the two signals with respect to the electron signal defines the time of flight of the neutron (t_n) with a combined resolution of $\Delta t_n = 1$ ns standard deviation. This corresponds to a momentum resolution $\Delta|\mathbf{p}_n|/|\mathbf{p}_n| = 4$ % at the front wall and 3 % at the rear wall. The overall detector thickness of 40 cm yields a neutron detection efficiency of $\epsilon_n = 32$ % at the average kinetic energy of quasi–elastic neutrons of ≈ 170 MeV. Thin plastic scintillators (thickness = 1 cm) in front of each neutron wall operate as veto counters for charged particles. The neutron detectors were shielded from electromagnetic background produced in the target region by 5 cm of lead (Fig. 4). 1 m–thick concrete walls shielded them from the electron beam line and dump.

3.3 The polarized ^{3}He target

The ^{3}He polarizer (Fig. 5) has been specially developed for this experiment and its principle has been described in [28,46,47]. It is a system of circulating ^{3}He gas. A LNA laser with a c. w. power of 5 W spin polarizes ^{3}He by optical pumping of metastable ^{3}He* atoms [48] in a low pressure (≈ 1 mbar) discharge in two large optical pumping cells (OPC) of volume 3 l. The polarized gas is compressed into the target cell ($p_t = 1$ bar, V = 100 cm^3) by means of a nonmagnetic Toepler compressor, which uses a liquid mercury piston. In order to compensate for relaxation of spin alignment in the target cell a continuous flow of 2 mbar·l/min ($\approx 10^{18}$ atoms/s) is circulated from the target cell, via capillary tubes and a getter purifier, back into the OPCs for repolarization.

^{3}He polarization within the OPCs was determined from the degree of circular polarization of fluorescence light, as measured by the so–called OPN unit [49,50] (Fig. 5), and a steady state polarization of $P_0 = 70$ % was achieved. The ^{3}He polarization P_t within the target cell was monitored by NMR. The NMR signal was calibrated periodically by returning a certain fraction of the gas directly into the previously evacuated OPCs and then performing the OPN measurement. An overall accuracy $\Delta P_t/P_t = 10$ % is estimated for this measurement [51].

The target polarization is reduced, with respect to that in the OPCs, by a factor [47]

$$P_t/P_0 = (1 - L)/(1 + T_C/T_1) \qquad (18)$$

due to a loss L = 13 % during compression and to the gas recycling time $T_C = 50$ min with respect to the spin relaxation time T_1. The relaxation rate $\Gamma_1 = 1/T_1$ is composed of 4 components:

(i) Dipolar coupling during ^{3}He–^{3}He collisions contribute, at 1 bar and T = 300 K, a rate $\Gamma_D = 1.2 \cdot 10^{-3}$ h^{-1} [52].

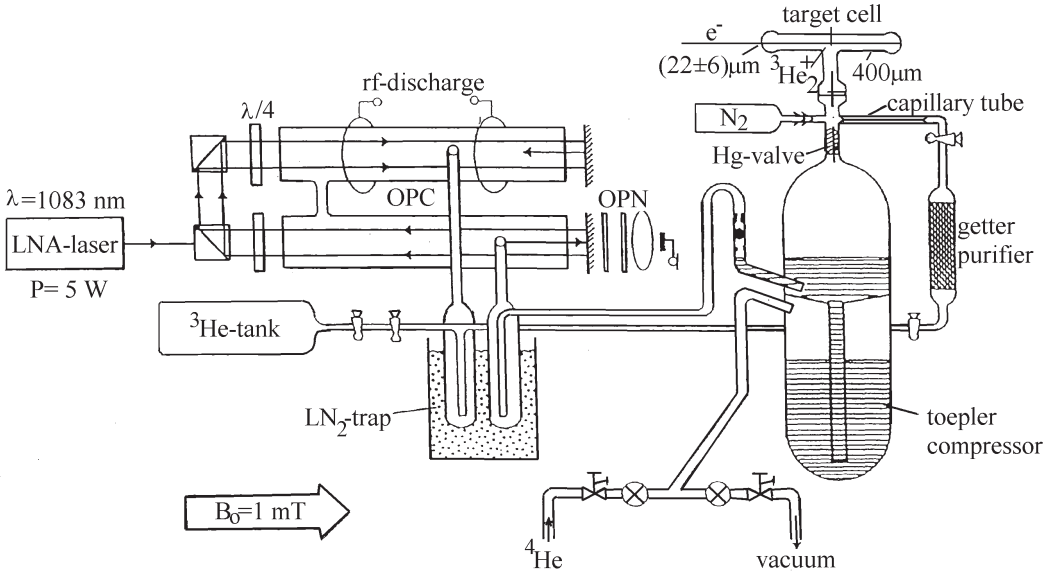

Fig. 5. Schematic of the setup to polarize ^{3}He

(ii) Diffusion through the transverse magnetic field gradient $\nabla_\perp B$ [53,54] causes a relaxation rate

$$\Gamma_\nabla = 1.7 \cdot 10^4 \left(\frac{\nabla_\perp B}{B}\right)^2 \frac{1}{p_t} \frac{\mathrm{cm^2\,bar}}{\mathrm{h}}. \qquad (19)$$

At 1 bar and a measured relative gradient of $4 \cdot 10^{-4}$ cm^{-1} at the target position, this term contributes a rate $2.7 \cdot 10^{-3}$ h^{-1}.

(iii) A potentially serious source of relaxation is the formation of $^3He_2^+$ molecules by the electron beam. They relax the nuclear spin promptly through coupling to the angular momentum J and, moreover, they act catalytically due to the fast exchange of atoms during collisions [55,56]. At the given current and ^{3}He density they are formed at a rate of $5 \cdot 10^{14}$ cm^{-1}sec^{-1}. Following [55,56] we have quenched them by admixing 0.1 mbar of nitrogen to the compressed ^{3}He. The corresponding ratio of 0.0014 of neutrons expected from scattering from N_2 and ^{3}He is negligible. The residual relaxation rate is given approximately by [57]

$$\Gamma_{He_2^+} = 5.7 \cdot 10^3 \cdot i \, \frac{1}{\mathrm{h} \cdot \mu\mathrm{A}}. \qquad (20)$$

Inserting the average beam current yields $\Gamma_{He_2^+} \approx 0.04$ h^{-1}.

(iiii) The dominant component is due to collisions with the walls of the container and hence is proportional to its surface to volume ratio

$$\Gamma_{\mathrm{wall}} = \gamma S/V\,. \qquad (21)$$

For supremax glass the characteristic coefficient γ is in the order of 0.2 h^{-1} cm [54]. It limited T_1 to 3 h and hence P_t to 40 % during the pilot run [28]. A decisive improvement has been achieved by coating the walls with *Cs* which yielded up to 117 h for closed–off spherical supremax cells [54]. For the complex geometry and running conditions of the target cell we achieved $T_1 = 6$ h by *Cs* coating [51].

A further improvement resulted from reducing the piston – stroke period of the Toepler compressor from 29 s to 24 s. At constant $T_C = 50$ min this allowed a reduction of the gas pressure in the OPCs from 1.3 mbar to 1.1 mbar which raised the polarization P_0 from 64 % to 70 % [51]. The combination of these measures yielded a substantial improvement of the target polarization from 40 % to 50 %.

A guiding magnetic field $B_0 = 1$ mT determined the spin direction in the OPCs and the target cell. It defined the orientation of the target spin for the asymmetry measurement in geometry $A_\perp$, where the target spin was aligned perpendicular to the calculated average momentum transfer. To measure the asymmetry in parallel geometry ($A_\parallel$) the target spin was rotated through 90^o by an additional pair of Helmholtz coils wound around the target only. Asymmetries $A_\perp$ and $A_\parallel$ were measured alternately for periods 60 min and 10 min, respectively. Since ^{3}He recycling has to be stopped for the latter measurement, P_t drops during this time by 4 % (relative) and recovers thereafter in the perpendicular phase, when freshly polarized gas is cycled again into the target cell. It was verified that the average target polarization was equal in both phases. Since this also held for the beam polarization, the product $P_e P_t$ cancels in the ratio of asymmetries (17) to a systematic uncertainty of ±0.5 % (see Table 3, row 8).

The alignment of the target spin in the scattering plane to which the obtained G_{En} number is sensitive has been improved substantially, as compared to the pilot experiment [28]. This was achieved by compensating for the earth's magnetic field, by repeatedly checking the field

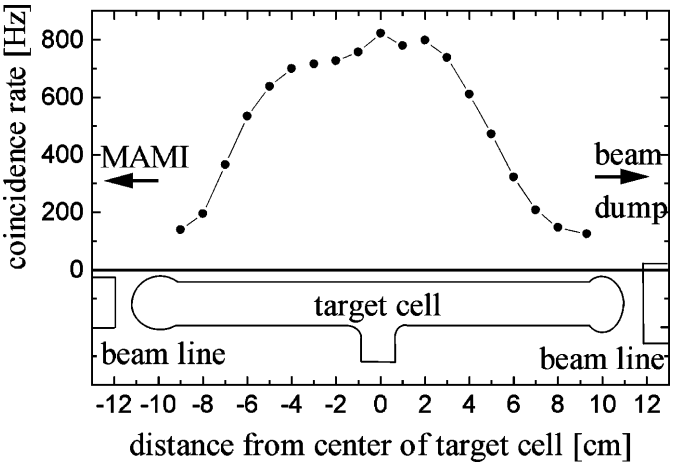

Fig. 6. Coincidence rate of the focussing Čerenkov- and the lead glass detector as function of displacement of the test target foil from the center position. The background of about 100 Hz in this test measurement consists of scattering from air and of accidental coincidences and is dependent on the photo multiplier voltage

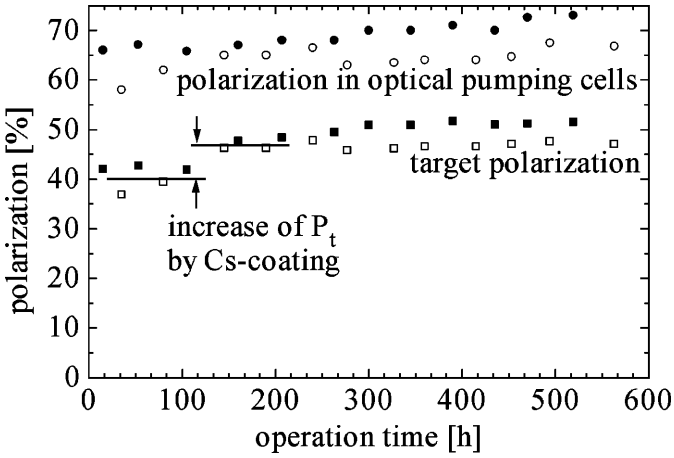

Fig. 7. ^{3}He polarization in the target cell and optical pumping cells during 563 hours of running. Open and full symbols represent measuring periods of 20 hours with alternating sign of P_t

alignment during the measuring phase, and by monitoring all field generating currents in apparatus adjacent to the target [51]. The final uncertainty was 0.2^o which resulted in a 3.0 % contribution to the systematic error (see Table 3, row 7).

In order to minimize the background level in the data the glass, entrance and exit windows of the target cell were etched with *HF* down to (22 ± 6) μm thickness. The glass side walls were similarly reduced to 400 μm. 20 μm thick *Be* foils were used as exit and entrance windows of the electron beam line before and after the target cell.

4 Data taking

4.1 Auxiliary measurements

The vertex selection by the focussing Čerenkov detector (Fig. 6) was checked by substituting a 700 μm *Al* foil for the target cell and scanning it along the beam direction. The lead glass – Čerenkov coincidence rate was registered as a function of foil position for various gain settings of the Čerenkov. The background rate of $\approx$ 100 Hz has to be subtracted. It results from scattering from surrounding air and from accidental coincidences between Čerenkov- and lead glass detector ($\approx$ 40 Hz). The lower part of Fig. 6 shows the corresponding positions of the ^{3}He target cell and beam windows. The detection efficiency is nearly 1 in the center. It drops to zero 2 cm inside the target cell and thus effectively inhibits background from the windows. The effective target length is about 10 cm. The vertex response function defined by the Čerenkov response curve in Fig. 6 defines the spatial resolution of the vertex reconstruction and serves as input for the Monte Carlo simulation of data presented in Sect. 5.4. Further measurements with empty target cells and with cells filled with H_2 or D_2 were made to determine potential sources of background [58,51]. The empty target cell measurement proved that the contribution from scattering in the windows is negligible. By comparing the $H(e, e'p) \rightarrow Pb(p, n)$ signal with that of ^{3}He$(e, e'n)$ it was concluded that the two protons in ^{3}He may contribute to the $(e, e'n)$ signal, after (p, n) charge conversion in the lead wall of the neutron detector. This contribution may be limited to 4 % by tight time–of–flight (TOF) cuts (see Sect. 5.3).

4.2 Production runs

During the experiment lead glass, air Čerenkov, neutron triple coincidences were recorded at a rate of $\approx$ 30 Hz, of which $\approx$ 8 % were quasi–elastic scattering events. Further kinematic selection to reduce systematic errors reduced the subset of data employed to obtain G_{En} to $\approx$ 1.5 % of that recorded.

After 20 cycles of data taking in the kinematical settings $A_\perp$ and $A_\parallel$ (defined in Sect. 3.3) the sign of P_t was inverted in both phases for the next 20 cycles. This should cause a sign flip of both asymmetries and hence their ratio remains unchanged, which was confirmed within statistical uncertainties. This operation yielded an important check on the quality of the magnetic field alignment, which depends critically on proper compensation for the earth's field (compare [28]). In addition the sense of the circular polarization of the laser light was inverted by turning $\lambda/4$ plates by 90^o. Due to a hidden imperfection of optics the circular polarization seemed to be less perfect in one of the two settings resulting in a lower P_t (see Fig. 7). We recall that the slightest admixture of opposite light polarization seriously affects the optical pumping dynamics [47]. Nevertheless, this effect drops out in the analysis as in both settings $A_\perp$ and $A_\parallel$ change by the same amount.

Six runs between November 1994 and May 1995 spanned a total of 563 h of running, out of which 389 h

Table 1. Record of ^{3}He$(\mathbf{e}, e'n)$ runs

	Nov. '94	Dec. '94	Jan. '95	Mar. '95	Apr. '95	May '95	sum
data taking [h]	70	52	10	83	78	96	389
$\bar{i}$ [μA]	6.5	5.2	3	5.9	7.5	6.0	
Q [μAh]	456	270	30	490	585	576	2407
$\bar{P}_t$ [%]	40	47	48	49	49	49	
$\bar{P}_e$ [%]	31	31	31	45	50	52	
F=$Q\cdot\bar{P}_t^2\cdot\bar{P}_e^2$	7.0	5.3	0.7	22.9	33.7	35.9	106

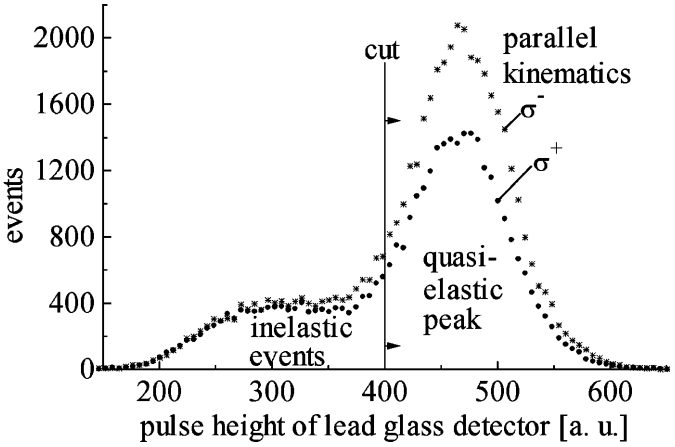

Fig. 8. The pulse height spectra of the lead glass detector modified for the purpose of separating elastic from inelastic events are shown for helicity states σ^+ and σ^-, respectively, as measured in parallel geometry

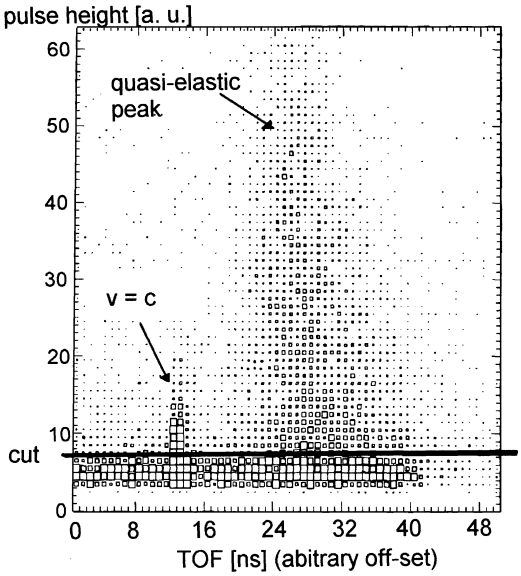

Fig. 9. Two dimentional plot of pulse height versus TOF for one scintillator bar. Events falling below the horizontal line are rejected

were used for production data taking. The relevant parameters are listed in Table 1. The rise of P_t due to *Cs* coating of the target cell occured after the first run. Even more important was the rebuilding of the polarized electron source between January and March 1995, resulting in a much more stable operation and an enhancement of the beam polarization from 30 % to 50 %. These improvements are shown in the so–called quality factor F which is the product of the beam integral Q and the square of the two polarizations. It represents the statistical weight of a run. The last three clearly contribute dominantly.

5 Analysis

5.1 Detector calibration

Signal amplitudes from the lead glass calorimeter modules were calibrated and analysed for each 20 h period so that for the sum signal Fig. 8 the peak of the quasi–elastic distribution fell at the same position on the spectrum, irrespective of electron scattering angle (and hence energy). This was done to aid the separation of quasi–elastic and inelastic events (Sect. 5.3).

A TOF spectrum is shown for one scintillator bar of the TOF array in Fig. 9 as a two-dimensional plot of mean pulse height versus walk-corrected mean TOF. The quasifree scattered neutrons fill the large region between 24 ns and 40 ns. A second, 2 ns–wide peak at 13 ns belongs to prompt (e', γ) coincidences from inelastic events in the target which are characterized by the sharp minimum TOF. The parameters for the walk corrections were optimized to minimize the width of this peak. Then its width can be taken as a measure for the time resolution of the coincidence, whereas its position can be used to obtain the time–zero point of each TOF spectrum. This calibration was checked off–line for each 100 h running period. Figure 9 also shows an uncorrelated background of events with low pulse height, which is largely removed by application of a suitable pulse height threshold.

To obtain the final energy and momentum resolution of a reconstructed neutron event the angular and TOF resolutions of the n-detectors, given in Sect. 3, have to be folded with the vertex response function of the Čerenkov counter, shown in Fig. 6. The modest TOF resolution $\Delta t/t \approx 1$ ns/25 ns leads to a correspondingly large standard deviation of 15 MeV for the extracted energy T_n of a neutron event. Uncertainty of the zero–point of 0.25 ns leads to a systematic calibration error of T_n of 3.6 MeV or 2 % (relative). The much better angular resolution of

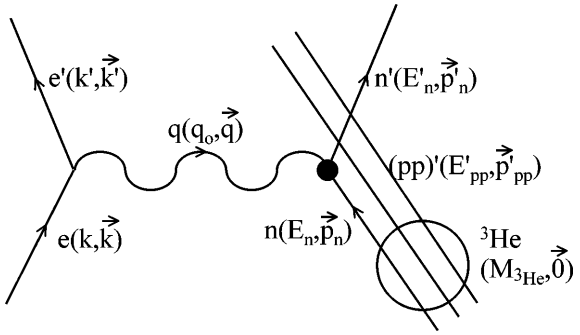

Fig. 10. Reaction mechanism for kinematical reconstruction of the ^{3}He$(e, e'n)pp$ reaction

the detector does not enhance significantly the width of the T_n determination.

5.2 Reconstruction of event kinematics in the PWIA approximation

The reconstruction of event kinematics of the ^{3}He$(e, e'n)pp$ reaction from the particular observables of our detector system was developed originally [60] for the purpose of a refined analysis of our pilot experiment [28]. The present analysis follows these lines. The experiment yields five kinematic observables, from which a ^{3}He$(e, e'n)pp$ event may be reconstructed. These are the three components of the final neutron momentum vector $\mathbf{p}'_n$ and the two angles of the unit vector $\hat{\mathbf{k}}'$ of the final electron momentum $\mathbf{k}'$. A sixth variable, the final electron energy E', was not used as the modest energy resolution did not offer any significant additional constraints.

In the first step of the analysis we reconstruct the kinematics of each event from these five observables in the PWIA (see Fig. 10) with the additional approximation: three unobserved minor contributions to the energy balance are neglected:

(i) The missing energy E_{miss}, which is in this case the kinetic energy of the two protons in their common rest frame.
(ii) Radiative energy loss of the electron in the scattering process.
(iii) Energy loss of the knocked out neutron in the lead shield on its way to the detector.

Following references [31,32,60] we reconstruct k' and calculate the decisive four momentum transfer

$$q_\mu = k_\mu - k'_\mu = (p'_n)_\mu - (p_n)_\mu \tag{22}$$

by exploiting energy and momentum conservation

$$M_{^3He} + k = k' + E'_n + E'_{pp} \tag{23}$$

$$\mathbf{0} + \mathbf{k} = k'\hat{\mathbf{k}}' + \mathbf{p}'_n + \mathbf{p}'_{pp}. \tag{24}$$

(We use natural units and treat the electron in the relativistic limit $E = k$, $E' = k'$.) Using approximation (i) we can express the energy of the final (pp) system E'_{pp} by the rest mass $2M_p$ and their momentum p'_{pp}:

$$E'_{pp} = \sqrt{(2M_p)^2 + {p'_{pp}}^2}\,. \tag{25}$$

Formulas (23) to (25) represent five equations from which the five unobserved variables k', E'_{pp} and $\mathbf{p}'_{pp}$ are calculated, yielding in particular for the final electron momentum in terms of measured quantities

$$k' = \frac{(k + M_{^3He} - E'_n)^2 - (\mathbf{k} - \mathbf{p}'_n)^2 - 4M_p^2}{2 \cdot ((k + M_{^3He} - E'_n) - (\mathbf{k} - \mathbf{p}'_n)\hat{\mathbf{k}}')}\,. \tag{26}$$

The standard deviation of the reconstructed k' is about 15 MeV or 2.3 % relative, mainly due to the neutron TOF resolution. Inserting the reconstructed k' value into (22) we obtain q_μ and the initial internal neutron momentum $\mathbf{p}_n$ for each event. The latter is required to transform to the rest frame of the initial neutron (see App. A) for which the asymmetry formula (8) applies.

In a second step of analysis we reconsider effects arising from approximations (i) to (iii) by applying averaged correction factors to the results of the above eventwise analysis (Sect. 5.6).

5.3 The selection of quasi–elastic events through kinematical cuts and discussion of background

The selection of quasi–elastic events by kinematical cuts was performed with the following objectives:

– to reduce the fraction of inelastic and accidental events in the signal to a level where their influence on the asymmetry can safely be quantified and partly corrected for.
– to reject events in the wings of the quasi–elastic peak which have initial internal neutron momenta too high to justify the use of the PWIA. We have set un upper limit of $|\mathbf{p}_n| = 100$ MeV/c.

The first cut applies to the neutron pulse height as discussed in Sect. 5.1 and shown in Fig. 9. Two further cuts concern the difference between the final neutron momentum $\mathbf{p}'_n$ and the reconstructed momentum transfer $\mathbf{q}$. They are applied to the longitudinal neutron momentum $\mathbf{p}'_{n\|}$ along $\hat{\mathbf{q}}$ and to the angle γ between $\hat{\mathbf{p}}'_n$ and $\hat{\mathbf{q}}$

$$|\mathbf{p}'_{n\|} - \mathbf{q}| = |\mathbf{p}_{n\|}| \leq 60 \text{ MeV/c} \tag{27}$$

$$\gamma = \angle(\hat{\mathbf{p}}'_n, \hat{\mathbf{q}}) \leq 6^o\,. \tag{28}$$

First of all these conditions restrict the accepted momentum of the bound neutron to

$$p_n \leq 100 \text{ MeV/c} \tag{29}$$

cutting out the wings of the neutron momentum wave function, which has a full width at half maximum of $\Delta p_n = 123$ MeV/c [27]. In addition, the 6^o cut effectively suppresses inelastic and accidental events since the tight

$(\hat{\mathbf{p}}'_n, \hat{\mathbf{q}})$ angular correlation, characteristic of quasi–elastic scattering, is missing there.

The electron pulse height spectrum of events with these restrictions applied is shown in Fig. 8. The quasi–elastic peak is distinct from a four times smaller shoulder of residual inelastic events. The two curves correspond to positive and negative electron helicity, respectively, with the $^3\mathbf{He}$ spin aligned parallel to $\mathbf{q}$. We observe a strong $A_\parallel$–asymmetry in the quasi–elastic peak which vanishes in the shoulder of inelastic events. Rejection of events below channel 400 in Fig. 8 restricts the fraction of inelastic events in the data set to a tolerable level of 4 %, as discussed below.

These four cuts suppress background from the dominant $^3\mathbf{He}(\mathbf{e}, e'p)$ reaction efficiently. This background arises from the proton converted in the lead wall to a neutron and then being detected as such. Due to the large average energy loss of protons in the lead before conversion these events appear with retarded TOF producing $\mathbf{p}'_{n\parallel}$ values too small to fulfill (27). The sensitivity to (p, n) conversion has been investigated quantitatively in runs with gaseous [58] and liquid [59] H_2–targets. We conclude from these tests that (p, n) conversion produces a residual background of 4 % which contributes to the asymmetry, since the protons carry a polarization P_p [30], dependent on the internal proton momentum p_p. $P_p/P_{^3He}$ is about -12 % at the quasi–eleastic peak but changes sign at $p_p \approx 70$ MeV/c. The protons converted into neutrons in the data set have on average higher initial momenta than reconstructed, since they suffer the unobserved energy loss in the lead before being detected. We conclude that the average polarization of (p, n) converted events can be estimated, with a 1σ error, to be $-5\,\% \leq \bar{P}_p \leq 5$ %. Since the proton has a large A_I value of 0.36 [41] in this Q^2 range this background results in a 2.6 % systematic uncertainty in $A_\perp/A_\parallel$. This transforms to a systematic error of 2.3 % in the corrected final ratio (37) $A_{I,ex}/A_{S,ex}$ and hence in $G_{E,n}$ (compare [58,51], see Table 3, row 5).

Inelastic events apparently do not exhibit a significant asymmetry in parallel geometry, as seen from the vanishing difference in the inelastic shoulder in Fig. 8. In perpendicular geometry, on the other hand, the asymmetry for inelastic events was found to be about the same as for quasi–elastic ones. This false asymmetry thus causes an error in $A_\perp/A_\parallel$ in proportion to the residual fraction of inelastic events in the data set. This fraction can be estimated by comparing the measured parallel asymmetry $A_\parallel$ to the expected one, calculated using (33) in Sect. 5.5. As mentioned in Sect. 2 and carried through in Sect. 5.5, the kinematical constants of A_S are virtually independent of the form factors. Hence they can be calculated using the formalism of Sect. 5.5 with the precision of 2 % of the kinematical reconstruction (see Table 3, row 10) yielding for the data with a parallel spin setting

$$A_\parallel = -69.3\,\%\, P_e\, P_{He}\, V. \tag{30}$$

Inserting the measured polarizations P_e and P_{He} of Table 1, with their respective relative errors of 5 % and 10 % (see Sects. 3.1 and 3.3) and the measured $A_\parallel$ values of Table 2, we obtain from this particular analysis a value for V and further through (14) a total background to signal ratio

$$B/S = (4.5 \pm 7.5)\,\%. \tag{31}$$

On the other hand we know from measurements that (p,n) conversion and accidental coincidences form (virtually unpolarized) backgrounds of 4 % each. Subtracting these fractions from the upper limit of 12 % in (31) leaves a 1σ upper limit for the contribution of inelastic events to the background of 4 %. This uncertainty generates an error of 4 % in $A_{I,ex}/A_{S,ex}$ (see Table 3, row 9) under the assumption that the magnitudes of the asymmetries of residual inelastic events do not exceed the values for quasi–elastic events.

With a suitably high neutron pulse height threshold applied accidental coincidences were found to have no significant influence on the measured asymmetry ratio.

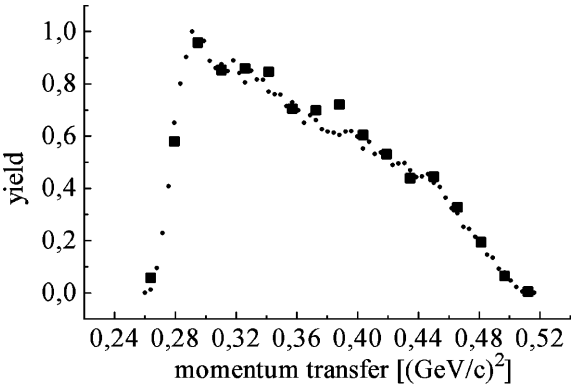

Fig. 11. Comparison of reconstructed 4–momentum transfer Q^2 (points) and the corresponding Monte Carlo simulation (squares)

5.4 Monte Carlo simulation

The Monte Carlo (MC) program CARLO.C was developed to simulate the detector response for quasi–elastic scattering [51,61]. The dipole form factor for G_{Mn} and the Platchkov result for G_{En}, evaluated with the Paris potential [14]

$$G_{En} = -1.25 \cdot \tau/(1 + 18.3 \cdot \tau) \cdot G_{Mn} \tag{32}$$

(see Fig. 13), served as input. To approximate the initial momentum distribution of the neutron in the ^{3}He nucleus a measured 3–body–breakup momentum distribution of the proton in ^{3}He [63] was used. Figure 11 gives an example for the correspondence of a measured spectrum and its simulated equivalent. This simulation was exploited in three phases of the analysis:

(i) The comparison of measurements and simulations helped to optimize kinematic cuts and to evaluate the residual background contributions.
(ii) The simulation helped to evaluate the error of and corrections to the event reconstruction caused by the

finite detector resolution, the large kinematic range covered and the different background contributions.

(iii) Missing energy, radiative loss and possible energy loss of a neutron in the lead shielding are not known a priori and hence have been neglected in the event–by–event kinematic reconstruction. Nevertheless, it was possible to calculate their average influence on the kinematics using the MC simulation, resulting in corrections to the asymmetries and to G_{En} (see section 5.6).

As to point (ii) the simulations resulted in a correction of the kinematic constants of (34) and (35) due to the finite detector resolution. Two sources dominate. The first concerns a shift of the centre of gravity of events 10 mm downstream of the origin of our coordinate system. This was caused by the asymmetric form of the vertex resolution function of the Čerenkov detector (see Fig. 6) which is a result of the strong dependence of the Mott cross section on the scattering angle. The second originates from a second order shift of the average neutron energy of about 1 MeV caused by the finite TOF resolution. The corrections sum up to +0.0009 in G_{En} (see Table 3, row 4).

The background, as discussed in Sect. 5.3, contributes somewhat skewed $\hat{\mathbf{q}}$ and Q^2 data to the eventwise reconstruction resulting in an error of the kinematical constants (34) and (35). Using the MC simulation the resulting error in G_{En} is estimated to be ± 2 % relative (see Table 3, row 10).

Further results of the MC simulation are quoted below.

5.5 Evaluation of asymmetries and extraction of G_{En}

We use the asymmetry formula (8), valid for elastic scattering from a free neutron, and account for the initial motion of the neutron by transforming the scattering process into the rest frame of the neutron for each event (App. A, (52)). This means that the kinematic constants $\tilde{a}, \tilde{b}, \tilde{c}, \tilde{d}$, (53)–(56), become explicitly dependent on the momentum $\mathbf{p}_n$, as reconstructed event–by–event in the PWIA approximation. This analysis [60] accounts accurately for variations in kinematics over the covered kinematic range as well as for any kinematics–dependent variation of the detector efficiency.

We obtain correct average asymmetries for a particular data set by averaging over the eventwise–reconstructed kinematic constants $\tilde{a}_i$, $\tilde{b}_i$, $\tilde{c}_i$, $\tilde{d}_i$. These give correct averages of G_{En} under the preliminary assumption that the asymmetry (52) is linear in G_{En}.

$$\langle A \rangle = P_e P_n V (\langle B \rangle + \langle C \rangle \; G_{En}) \tag{33}$$

The small G_{En}^2 term in the dominator of (52) is accounted for by iterating (33), with convergence achieved after one iteration. The coefficients $\langle B \rangle$ and $\langle C \rangle$ are the averaged contributions of A_S and A_I, respectively,

$$\langle B \rangle = \sum_{event\ i} \frac{\tilde{b}_i \cdot G_{Mn}^2(Q_i^2)}{\tilde{c}_i \cdot G_{En}^2(Q_i^2) + \tilde{d}_i \cdot G_{Mn}^2(Q_i^2)} \tag{34}$$

$$\langle C \rangle = \sum_{event\ i} \frac{\tilde{a}_i \cdot G_{Mn}(Q_i^2)}{\tilde{c}_i \cdot G_{En}^2(Q_i^2) + \tilde{d}_i \cdot G_{Mn}^2(Q_i^2)} \,. \tag{35}$$

Both are calculated separately for parallel ($\langle B_\parallel \rangle$, $\langle C_\parallel \rangle$) and for transverse ($\langle B_\perp \rangle$, $\langle C_\perp \rangle$) settings of the ^{3}He spin. Bearing in mind that the average $\mathbf{q}$ direction, and hence $\langle \Theta \rangle$, of a specific data set depends sensitively on the corresponding event selection, a residual contribution from the large asymmetry component A_S may cause a significant difference between $\langle A_\perp \rangle$ and A_I.

Inserting measured asymmetries $\langle A_\perp \rangle$ and $\langle A_\parallel \rangle$ into (33) and taking their ratio to eliminate $P_e P_n V$ we obtain for G_{En} in this first step of analysis

$$\langle G_{En} \rangle^{1.step} = \frac{\left(\langle A_\perp \rangle / \langle A_\parallel \rangle \right) \langle B_\parallel \rangle - \langle B_\perp \rangle}{\langle C_\perp \rangle - \left(\langle A_\perp \rangle / \langle A_\parallel \rangle \right) \langle C_\parallel \rangle} \,. \tag{36}$$

$\langle B_\perp \rangle$ and $\langle C_\parallel \rangle$ compensate for a possible average misalignment of the data sample from perpendicular or parallel geometry, but the effect of $\langle C_\parallel \rangle$ is negligible. The more important term $\langle B_\perp \rangle$ is related to the strong angular dependence of A at $\Theta = 90°$ (see Fig. 2). Omitting the $\langle C_\parallel \rangle$ term we may simplify (36) to

$$\begin{aligned} \langle G_{En} \rangle^{1.step} &= \left(\frac{\langle A_\perp \rangle}{\langle A_\parallel \rangle} - \frac{\langle B_\perp \rangle}{\langle B_\parallel \rangle} \right) \frac{\langle B_\parallel \rangle}{\langle C_\perp \rangle} \\ &= \left(\frac{A_{I,ex}}{A_{S,ex}} \right) \frac{\langle B_\parallel \rangle}{\langle C_\perp \rangle} \end{aligned} \tag{37}$$

were we have introduced the kinematically readjusted experimental asymmetry ratio $(A_{I,ex}/A_{S,ex})$. The analysis yields $(A_{I,ex}/A_{S,ex})$ = -0.1204±0.0114$_{stat}$ and through (37) for G_{En} a first step value

$$\langle G_{En} \rangle^{1.step}_{0.27 \le Q^2c^2/GeV^2 \le 0.5} = 0.0296 \pm 0.0033_{\mathrm{stat}} \tag{38}$$

to which corrections and systematic errors have still to be applied. The importance of readjusting the asymmetry ratio is seen from the comparison to the quite different uncorrected ratio $(A_\perp/A_\parallel)_{ex}$ = -0.073±0.011$_{stat}$. The difference is due to a tilting of the average $\hat{\mathbf{q}}$–vector by the various cuts (compare Fig. 2).

5.6 Kinematic corrections to G_{En}

The corrections to be discussed in this section are all due to the fact that we have not precisely measured the energy E' of the scattered electron but rely on its reconstruction from its measured direction $\hat{\mathbf{k}}'$ and the measured final neutron momentum $\mathbf{p}'_n$. This reconstruction ignores the following possible energy losses (compare Sect. 5.2), namely

(i) by transfer of energy to the relative motion of the protons (so-called missing energy),
(ii) by internal bremsstrahlung,
(iii) by inelastic neutron scattering in the lead wall.

Each of these three effects results in an on average overestimation of the reconstructed k' value and hence affects the reconstructed $\mathbf{q}$-vector. A small shift in $|\mathbf{q}|$ does not affect the analysis much, but the accompanying systematic tilt of its direction is important. This tilt is imposed by the experimentally fixed direction but unobserved magnitude of $\mathbf{k}'$. Since $\mathbf{k}'$ is almost perpendicular to $\mathbf{q}$ a false estimation of k' by e. g. $\Delta k' = 1$ MeV/c tilts $\mathbf{q} \approx 600$ MeV/c by an angle $\xi = 1/600$ rad causing an erroneous contribution from A_S to the perpendicular asymmetry of

$$\frac{\Delta \langle A_\perp \rangle}{\langle A_\perp \rangle} = \xi \cdot \frac{A_S}{A_I} = \frac{\Delta k'}{q} \frac{A_S}{A_I} \approx \frac{1}{600} \cdot 9 = 1.5\ \%\,. \quad (39)$$

MC simulation of neutron–energy–loss effects shows that on average this rotates $\hat{q}$ in the same direction as the k' effect. The tilting coefficients and corresponding sensitivities of G_{En} to energy losses (i)–(iii) have been determined quantitatively by MC simulation to be

$$\partial G_{En}/\partial E_{\rm miss} = 5.7 \cdot 10^{-4}/\text{MeV} \quad (40)$$
$$\partial G_{En}/\partial E_{\rm rad} = 2.1 \cdot 10^{-4}/\text{MeV} \quad (41)$$
$$\partial G_{En}/\partial T_n = 2.4 \cdot 10^{-4}/\text{MeV}\,. \quad (42)$$

G_{En} is less sensitive to radiation losses ($E_{\rm rad}$) than to missing energy ($E_{\rm miss}$) for two reasons.

1. Bremsstrahlung is peaked with roughly equal intensity along $\hat{k}$ and $\hat{k}'$ [62] but losses in the exit channel k' don't skew the reconstruction of $\mathbf{q}$.
2. Energy and momentum losses by bremsstrahlung are shared considerably between electron and neutron, whereas missing energy concerns fully k'.

The cut in the pulse height spectrum of the lead glass detector at channel 400 (see Fig. 8) rejects events with high radiation losses at an effective cut value of 90 MeV. The MC simulation predicts all of the sensitivities (40)–(42) to be constant in this accepted range of energy loss. The correction to G_{En} is then obtained simply by multiplying the average energy loss $\bar{E}_i$ with the corresponding sensitivity and the need for an eventwise correction is avoided.

Experimental information on the missing energy spectrum for quasi–elastic scattering on ^{3}He exists only for the $^3\text{He}(e, e'p)pn$ channel [63–65]. The most recent experiment [64], which comes closest to our kinematics, yields an average missing energy of 2.8 MeV, where the upper integration limit was about 20 MeV. This value is consistent with the older measurements [63,65].

The problem has also been studied in a recent Faddeev calculation which considered FSI effects [27]. The authors have been provided with the complete kinematical response function of our experiment and have applied the same cuts in phase space as described in section 5.3. For the $(e, e'p)pn$ channel the calculation gives an average missing energy $\bar{E}_{\rm miss} = 3.0$ MeV, integrated over the entire spectrum, which is in good agreement with the experimental result. For the $(e, e'n)pp$ channel a somewhat smaller value of

$$\bar{E}_{\rm miss} = 2.6 \pm 0.3\ \text{MeV}\,. \quad (43)$$

was obtained, which has been adopted here. We estimate that the uncertainty is 10 %. Multiplying this value by sensitivity (40) leads to an increase of G_{En} by (Table 3, row 1)

$$\Delta G_{En,\rm miss} = 0.0015 \pm 0.0002\,. \quad (44)$$

Radiative losses have been studied in the kinematic range of the present experiment at NIKHEF and MAMI for $(e, e'p)$ experiments [64,62]. Since these losses depend only on the electron kinematics [66] the findings of [64,62] apply equally well to the $(e, e'n)$ reaction. Integrating up to a maximum loss of 90 MeV we obtain an average radiation loss of

$$\Delta E_{\rm rad} = (5.4 \pm 1.0)\ \text{MeV}\,, \quad (45)$$

which applied to sensitivity (41) yields the correction (Table 3, row 2)

$$\Delta G_{En,\rm rad} = 0.0011 \pm 0.0003\,. \quad (46)$$

We mention that external radiation losses in the two windows ahead of the target are negligible.

The energy loss of neutrons in the lead wall is calculated from neutron scattering data at equivalent energies [67,68]. At an average kinetic energy of $\bar{T}_n = 180$ MeV the reaction cross section is 1.7 barn. Thus 25 % of the neutrons experience a reaction in the 5 cm thick lead wall. The average energy loss is 20 MeV and the average scattering angle is 8^o [68]. Distances from the lead wall to the neutron detectors amount to 23 % and 41 % of the total neutron flight path for the first and the second wall respectively, so that scattering angle effects on $\mathbf{p}'_n$ are small and the resulting effect on the TOF is suppressed. For the same reason effects of elastic neutron scattering on the event reconstruction are negligible. Weighted by the relative count rates of the respective walls the respective suppression factors reduce the average energy loss per neutron from the true value of 4 MeV to an effectively observed value of

$$\Delta T_{n,\rm lead} = (-1.3 \pm 0.5)\ \text{MeV}\,. \quad (47)$$

This increases G_{En} according to sensitivity (42) by (Table 3, row 3)

$$\Delta G_{En,\rm lead} = 0.0003 \pm 0.0001\,. \quad (48)$$

Also through sensitivity (42) the TOF calibration uncertainty of 0.25 ns (see Sect. 5.1) results in a systematic error of G_{En} of ± 0.0009 (see Table 3, row 6).

5.7 Consistency checks of the analysis

To check the reconstruction formalism of Sect. 5.2 the data set was divided into two subsets on the basis of the value of a kinematic parameter. This was done separately for 4 parameters: reconstructed Q^2 (see Fig. 11), electron scattering angle ϑ_e, pulse height in the lead glass detector (see Fig. 8) and neutron kinetic energy T_n. The cuts were chosen to obtain equal statistical accuracy from each subset, namely at the following dividing values:

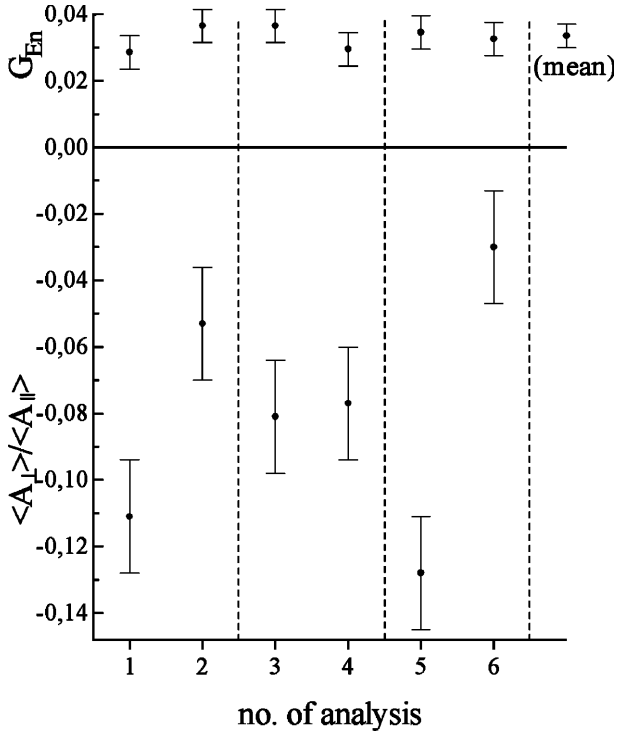

Fig. 12. Measured asymmetry ratios and resulting G_{En} values for the subsets Q^2<0.35 (GeV/c)^2 (1), Q^2>0.35 (GeV/c)^2 (2), electron pulse height channel $\leq$ 472 (3), electron pulse height channel $>$ 472 (4), $T_n < 178$ MeV (5), $T_n > 178$ MeV (6) and the mean of G_{En} (right). The error bars show statistical uncertainties

$Q^2 = 0.35(\mathrm{GeV/c})^2$, $\vartheta_e = 46^o$, electron pulse height channel 472 and $T_n = 178$ MeV. Measured asymmetry ratios $\langle A_\perp \rangle / \langle A_\parallel \rangle$ and resulting G_{En} values are shown for each subset in Fig. 12 together with the mean of G_{En}. The cuts in ϑ_e are omitted since they yield results identical to those from cutting on Q^2. Only statistical errors are shown in the plot. The asymmetry ratios of the different subsets differ significantly as a consequence of different contributions of A_S in perpendicular geometry. Considering for example the binning in T_n, the two subsets contain predominantly events with higher or lower momentum transfer q. Since the $\mathbf{q}$ vector turns to the forward direction as its magnitude increases, i.e. towards $\Theta < 90^o$ in perpendicular geometry, $\langle A_\perp \rangle$ is diminished by an admixture of A_S (compare Fig. 2) in accordance with the experiment.

However, for all subsets of Fig. 12 the readjusted asymmetry ratios and corresponding G_{En} values (see (37)) are consistent. Variations about a constant mean value produce a χ^2 of 0.54 per degree of freedom. This strongly supports the reliability of the reconstruction formalism. The largest variance of 20 % is found for the binning in Q^2 (no. 1,2). This variance far exceeds any systematic uncertainty of the reconstruction of the $\mathbf{q}$–vector, the influence of which is limited to a few percent (see Table 3) due to the tight kinematic restriction about the centre of the quasi–elastic peak. Neither could an unexpected dependence of the kinematic corrections of Sect. 5.6 on Q^2 explain a shift of this size. It would for example require a difference in missing energy between the two subsets of 14 MeV, whereas its total is only 2.6 MeV on average. In principle, G_{En} itself could change within this Q^2 interval, but a 20 % shift is unlikely over this range (see Fig. 13). On the other hand, the difference in the two Q^2 bins may reflect a strong Q^2 dependence of the FSI quenching of G_{En} (see Sect. 6). However, the statistical significance of this interpretation is marginal.

Summarizing we are led by these checks to conclude that the kinematic reconstruction of events is valid.

5.8 Integral analysis

An alternative mode of analysis operates directly on simple spectra, thus circumventing the kinematical reconstruction of individual events. This method was used for the pilot experiment [28] and preliminary quasi on–line analyses of the present data [69,70]. In the latter case, the validity of this procedure was much less certain, since averages had to be taken over the much wider kinematical acceptance of the full detector setup. In addition, with improved precision, it was important to minimize systematic uncertainties. Although superseded by the eventwise analysis we wish to comment on previously communicated preliminary results [69–71] and in doing so provide another, partly independent, insight into the consistency of the data and their analysis.

In the integral analysis the selection of quasi–elastic events proceeds along the lines of Sect. 5.3, except that the cuts on the primary neutron momentum $\mathbf{p}_n = \mathbf{p}'_n - \mathbf{q}$ are replaced by a cut on the neutron time of flight, since the former requires the reconstructed $\mathbf{q}$–vector. In the next step one calculates average $\bar{\hat{q}}$ and $\bar{Q}^2$ values from the measured angular distribution of scattered electrons $\hat{k}'$. Assuming a random distribution of $\mathbf{p}_n$ the mean value is set to $\bar{\mathbf{p}}_n = \mathbf{0}$. An average $\bar{\Theta} = \angle(\hat{P}_n, \bar{\hat{q}})$ and average kinematical constants a, b, c, d (8) with respect to $\bar{Q}^2$ were then obtained. Consequently G_{En} was evaluated with (8) as if the struck neutron was free and at rest.

The first comparison of integral and eventwise analysis [60] applied to the data of the pilot run [28] yielded identical values for G_{En}, but a factor 3 smaller systematic error with the latter mode.

The preliminary integral analysis of 50 % of the full data obtained a raw value of the asymmetry ratio [69, 70] $(\langle A_\perp \rangle / \langle A_\parallel \rangle)_{\mathrm{raw}} = -0.147 \pm 0.013_{\mathrm{stat}}$, which has been interpreted without readjustment as $(A_{I,ex}/A_{S,ex})$ and hence has to be compared to the readjusted value of $0.1204 \pm 0.0114_{stat}$ of the present analysis. The relatively small difference tells that the aim to center the raw events around $\Theta = 90°$ is well achieved by the detector setup.

Since a reliable background rejection for the wide acceptance of the full detector setup requires an eventwise kinematic reconstruction we have tried an integral evaluation of G_{En} only for a restricted data set. This has passed all the cuts of Sect. 5.3, but with somewhat more generous cut limits and hence smaller statistical error. The result

$\langle G_{En} \rangle = 0.029 \pm 0.002_{\rm stat} \pm 0.005_{\rm syst}$ agrees very well with the first step value obtained from the eventwise evaluation (38) [71]. This supports the consistency of all steps of the analysis and implies that (8) may be linearized over the Q^2 range in question. Never the less the safer eventwise analysis yields a smaller systematic error (compare (51)) and hence forms the final result.

5.9 Result

The asymmetry with respect to a helicity reversal of the electron was measured in perpendicular and parallel geometry in the double–polarized exclusive reaction $^3\mathbf{He}(\mathbf{e}, e'n)$ in quasi–elastic kinematics to determine the electric form factor of the neutron G_{En}. The experiment covered the kinematic range $39^o \leq \vartheta_e \leq 59^o$, $0.27 \leq Q^2c^2/GeV^2 \leq 0.5$. Hence the measured asymmetries $\langle A_\perp \rangle$ and $\langle A_\parallel \rangle$ are admixtures of the asymmetry components A_I, originating from the interference of electric and magnetic amplitudes, and A_S from the spin–flip part of the cross section. To disentangle these components 90 % of the data (see Table 1) have been analysed by eventwise reconstruction of the kinematics in the PWIA approximation, with restrictions applied to the kinematic parameters. Table 2 lists the measured asymmetries for the 3 subsets of the data used for the eventwise analysis. From the weighted average of measured asymmetry ratios

$$\frac{\langle A_\perp \rangle}{\langle A_\parallel \rangle} = -0.0726 \pm 0.0114 \qquad (49)$$

the ratio of interference and spin–flip asymmetry components

$$\frac{A_{I,ex}}{A_{S,ex}} = -0.1204 \pm 0.0114 \qquad (50)$$

has been calculated using (37) and used to produce the first step value for G_{En} (38). Adding corrections and errors from Table 3 we obtain in the PWIA, assuming the dipole value of G_{Mn} (4))

$$\langle G_{En}(Q^2) \rangle_{0.27 \leq Q^2c^2/\mathrm{GeV}^2 \leq 0.5} = 0.0334 \pm 0.0033_{\rm stat} \pm 0.0028_{\rm syst}\,. \qquad (51)$$

Table 2. Asymmetries obtained by eventwise reconstruction and event selection of Sect. 5.3

beam time	$\langle A_\perp \rangle$ [%]	$\langle A_\parallel \rangle$ [%]	$\langle A_\perp \rangle / \langle A_\parallel \rangle$
March '95	1.19± 0.34	-15.0 ± 0.9	-0.079± 0.023
April '95	0.94± 0.30	-15.9 ± 0.7	-0.059± 0.019
May '95	1.36± 0.30	-16.8 ± 0.7	-0.081± 0.018

6 Discussion and outlook

In Fig. 13 the present result is compared with the data of Platch-kov et al. [14] which stem from a measurement of elastic $D(e, e')$ scattering over a wide range of Q^2. Those data have good precision, but the analysis was highly dependent on the choice of the nucleon–nucleon potential for calculating the deuteron wave function. The G_{En} values shown correspond to the Paris potential and the full line is a two parameter fit (32) to them. The broken lines represent fits which result from analyzing the data with various other realistic nucleon–nucleon potentials.

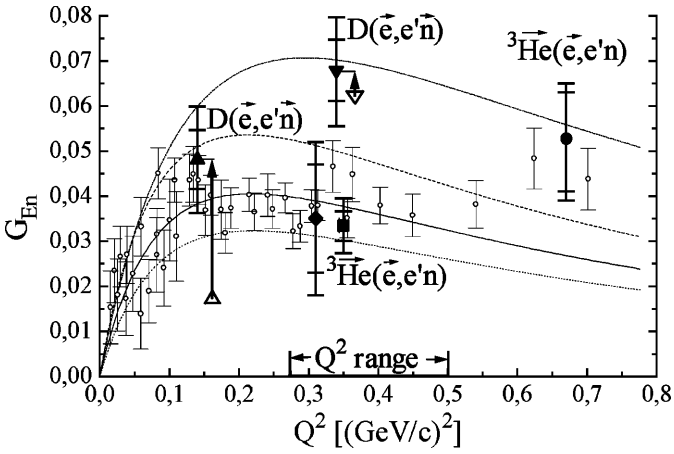

Fig. 13. A comparison of G_{En} values obtained using different reactions. $^3\mathbf{He}(\mathbf{e}, e'n)$: full square - present measurement; full diamond - the pilot experiment [28]; full circle - [61]. $D(\mathbf{e}, e'\mathbf{n})$: up triangles - [45,75]; down triangles - [44,45,75]. $D(e, e')$: open circles - [14], Paris potential analysis; full line - fit to Paris potential analysis; dotted line - Reid Soft Core potential fit; dashed line - Argonne V14 potential fit; dot–dashed line - Nijmegen potential fit. Inner error bars show statistical uncertainties. The up–arrows indicate the magnitudes of the FSI corrections applied to the $D(\mathbf{e}, e'\mathbf{n})$ results

Also shown are the two points [44,45] from a parallel measurement of G_{En} in doubly polarized $D(\mathbf{e}, e'\mathbf{n})$ scattering, performed in a similar kinematical range using the same detector system. These values are significantly higher than the present ^{3}He result. However the deuterium data have been corrected for FSI effects using the model of Arenhövel et al. [45,74,75]. This correction increases the points at $Q^2 = 0.15$ and 0.35 $(\mathrm{GeV/c})^2$ by amounts 0.0313 and 0.0054 respectively, showing the very strong Q^2 dependence of FSI effects. For ^{3}He we expect this correction to be significantly larger than for deuterium due to the presence of the second proton and the tighter binding. A Faddeev–type calculation of this effect is in progress [27]. A Q^2 dependence of the FSI quenching might also be reflected in the Q^2 binning of our data (see Fig. 12), although with marginal statistical significance.

At present it is still an open question whether the discrepancy between the results, obtained for ^{3}He and D, may be bridged by conventional nuclear structure corrections or whether a change of the intrinsic neutron structure due to medium effects has to be considered. In the case of the proton evidence for such an effect has been claimed [20] and later on denied [76]. However, the neutron is a much more sensitive probe, since the zero moment of the charge distribution vanishes G_{En} may be more

Table 3. Corrections and errors to G_{En} in absolute values and relative to the result (51)

row	source	primary correction/ error of source	influence on G_{En} absolute	influence on G_{En} relative	dealt with in Sect.
1	missing energy	(-2.6 ± 0.3) MeV	$+0.0015 \pm 0.0002$	$(+4.2 \pm 0.6)$ %	5.6
2	radiation loss	(-5.4 ± 1.0) MeV	$+0.0011 \pm 0.0003$	$(+3.3 \pm 0.9)$ %	5.6
3	energy loss in lead	(-1.3 ± 0.5) MeV	$+0.0003 \pm 0.0001$	$(+0.9 \pm 0.3)$ %	5.6
4	finite detector resolution		+0.0009	+2.7 %	5.4
5	proton polarization in ^{3}He		±0.0008	±2.3 %	5.3
6	TOF calibration	±0.25 ns	±0.0009	±2.6 %	5.1,5.6
7	spin alignment	$\pm 0.2^o$	±0.0010	±3.0 %	3.3
8	shift of target polarization between settings of target spin	±0.5 %	±0.0002	±0.5 %	3.3
9	shift of asymmetry ratio due to inelastic events		±0.0013	±4 %	5.3
10	shift of kinematical reconstruction by background		±0.0007	±2 %	5.4,5.5
11	G_{Mn} from world data	±5 %	±0.0017	±5 %	1
12	sum of corrections		+0.0038	+11.4 %	5.9
13	systematic error added in quadrature		±0.0028	±8.4 %	5.9
14	statistical error		±0.0033	±9.9 %	5.9
15	total error added in quadrature		±0.0043	±12.9 %	5.9

sensitive to nuclear binding. A reduction of G_{En} in proportion to the nucleon density in nuclear matter has been predicted by several calculations [19–21].

At larger Q^2, however, the FSI quenching is expected to be much smaller as mentioned. Therefore, the value derived from a $^3\mathbf{He}(\mathbf{e}, e'n)$ measurement at $Q^2 = 0.67(\mathrm{GeV/c})^2$ by a Mainz–Basel collaboration [61] is in good accord with the overall trend suggested by the recent results from the $D(\mathbf{e}, e'\mathbf{n})$ reaction achieved at MAMI. The calculations of [27] are urgently awaited in order to see whether the result of this paper will merge into the new trend.

This work has been granted by the Deutsche Forschungsgemeinschaft in the framework of the Sonderforschungsbereich 201 and of the Gradu-iertenkolleg Mu 705/3, by the Bundesministerium für Wissenschaft und Forschung under contract number 06 Tü 669, by the DAAD (313 ARCXII) and by the U. K. Engineering and Physical Sciences Research Council.

Appendix

A Covariant form of the asymmetry formula

The asymmetry of each scattering process is analysed in the rest frame of the initial neutron using the general covariant form of the asymmetry formula calculated on the basis of [31,32]

$$A = P_e P_n V \frac{\tilde{a}\, G_{En}(Q^2) G_{Mn}(Q^2) + \tilde{b}\, G_{Mn}^2(Q^2)}{\tilde{c}\, G_{En}^2(Q^2) + \tilde{d}\, G_{Mn}^2(Q^2)} \qquad (52)$$

with the kinematical constants

$$\tilde{a} = \frac{(qS^n)}{4M}[(qS^e)(qp^n) - q^2(S^e p^n)]$$

$$-\frac{M(1+\tau)}{2}[(qS^e)(qS^n) - q^2(S^e S^n)] \qquad (53)$$

$$\tilde{b} = \frac{-(qS^n)}{4M}[(qS^e)(qp^n) - q^2(S^e p^n)] \qquad (54)$$

$$\tilde{c} = \frac{1}{m}[M^4\tau - (p^n k)(p^n k')] \qquad (55)$$

$$\tilde{d} = \frac{\tau}{m}[M^4(\tau + 2\tau^2) - (p^n k)(p^n k')] \qquad (56)$$

which consist of Lorentz scalars formed from the 4–vectors: momentum transfer q, initial and final momentum of the electron k and k', respectively, the initial neutron momentum p^n and the spins of incident electron S^e and of the initial neutron S^n. Indices μ for the 4–vectors are omitted for simplicity. The 4–vector of a spin $\mathbf{S}$ is defined in the rest frame of the particle as $(0, \mathbf{S})$ and by Lorentz transformation in any other frame. Further scalars are the neutron rest mass M and $\tau = Q^2/(4M^2) = -q^2/(4M^2)$.

References

1. S. Boffi, C. Giusti and F. D. Pacati, Physics Reports **226**, 1 (1993)
2. F. J. Ernst, R. G. Sachs and K. C. Wali, Phys. Rev. **119**, 1105 (1960)
3. P. E. Bosted, Phys. Rev. C **51**, 409 (1995)
4. G. Quéméner et al., in *Proc. of the Int. Nucl. Physics Conf.*, INPC, Paris, France, 1998
5. H. Anklin et al., Phys. Lett. B **336**, 313 (1994)
6. H. Anklin et al., Phys. Lett. B **428**, 248 (1998)
7. E. E. W. Bruins et al., Phys. Rev. Lett. **75**, 21 (1995)
8. H. Gao et al., Phys. Rev. C **50**, R546 (1994)
9. P. Markowitz et al., Phys. Rev. C **48**, R5 (1993)
10. J. Jourdan et al., Phys. Rev. Lett. **97**, 5186 (1997)
11. E. E. W. Bruins et al., Phys. Rev. Lett. **79**, 5187 (1997)

12. S. Kopecky et al., Phys. Rev. C **56**, 2229 (1997)
13. A. Lung et al., Phys. Rev. Lett. **70**, 718 (1993)
14. S. Platchkov et al., Nucl. Phys. A **510**, 740 (1990)
15. S. Galster et al., Nucl. Phys. B **32**, 221 (1971)
16. T. Eden et al., Phys. Rev. C **50**, R1749 (1994)
17. C. E. Woodward et al., Phys. Rev. C **44**, R571 (1991)
18. A. K. Thompson et al., Phys. Rev. Lett. **68**, 2901 (1992)
19. U.–G. Meissner, Phys. Rev. Lett. **62**, 1013 (1989)
20. Il-Tong Cheon and Moon Taeg Jeong, J. Phys. Soc. Japan **61**, 2726 (1992)
21. D. H. Lu et al., Phys. Lett B **441** (1998) 27 and Phys. Lett. B **417**, 217 (1998)
22. J. M. Laget, Phys. Lett. B **273**, 367 (1991)
23. J. M. Laget, Phys. Lett. B **276**, 398 (1992)
24. R. Milner, Spin 94 conference, Bloomington (Indiana/USA), Sept. 1994
25. E. J. Brash et al., Phys. Rev. C **47**, 2064 (1993)
26. H. R. Poolman, Ph.D. thesis, Vrije Universiteit, Amsterdam, The Netherlands, 1999
27. W. Glöckle and G. Ziemer, Ruhr–University, Bochum, Germany (private communication)
28. M. Meyerhoff et al., Phys. Lett. B **327**, 201 (1994)
29. R. W. Schulze und P. U. Sauer, Phys. Rev. C **48**, 38 (1993)
30. R. Milner et al., Phys. Lett. B **397**, 67 (1996)
31. B. Blankleider and R. M. Woloshyn, Phys. Rev. C **29**, 538 (1984)
32. T. W. Donnelly and A. S. Raskin, Ann. Phys. (N.Y.) **169**, 247 (1986)
33. K. Aulenbacher et al., Nucl. Instr. and Meth. A **391**, 498 (1997)
34. M. Steigerwald et al., in *Proc. to the 12th Int. Symposium on High–Energy Spin Physics*, Amsterdam, The Netherlands, Sept. 1996, World Scientific, p. 743
35. K. H. Steffens et al., Nucl. Instr. and Meth. A **325**, 378 (1993)
36. H. Hartmann, diploma thesis, University of Mainz, Germany, 1990
37. M. Steigerwald, diploma thesis, University of Mainz, Germany, 1994
38. W. Heil et al., Nucl. Phys. B **327**, 1 (1989)
39. H. Schmieden, in *Proc. to the 12th Int. Symposium on High–Energy Spin Physics*, Amsterdam, The Netherlands, Sept. 1996, World Scientific, p. 819
40. J. Ahrens, University of Mainz, Germany (private communication)
41. D. Eyl, Ph.D. thesis, University of Mainz, Germany, 1993
42. J. R. M. Annand et al., Nucl. Instr. and Meth. A **262**, 329 (1987)
43. P. Grabmayr et al., Nucl. Instr. and Meth. **402**, 85 (1998)
44. M. Ostrick, Ph.D. thesis, University of Mainz, Germany, 1998 and submitted to Phys. Rev. Lett
45. C. Herberg, Ph.D. thesis, University of Mainz, Germany, 1998 and submitted to the Euro. Phys. J. A
46. M. Meyerhoff, Ph.D. thesis, University of Mainz, Germany, 1994
47. G. Eckert et al., Nucl. Instr. and Meth. A **320**, 53 (1992)
48. F. D. Colegrove, L. D. Schearer and G. K. Walters, Phys. Rev. **132**, 2561 (1963)
49. N. P. Bigelow et al., J. Phys. II France **2**, 2159 (1992)
50. W. Lorenzon et al., Phys. Rev. A **47**, 468 (1993)
51. J. Becker, Ph.D. thesis, University of Mainz, Germany, 1997
52. N. R. Newbury et al., Phys. Rev. A **48**, 4411 (1993)
53. L. D. Schearer and G. K. Walters, Phys. Rev. A **139**, 1398 (1965)
54. W. Heil et al., Phys. Lett. A **201**, 337 (1995)
55. K. D. Bonin, T. G. Walker and W. Happer, Phys. Rev. A **37**, 3270 (1988)
56. K. D. Bonin, D. P. Saltzberg and W. Happer, Phys. Rev. A **38**, 4481 (1988)
57. V. Kniese, diploma thesis, University of Mainz, Germany, 1992
58. K. Beuchel, diploma thesis, University of Mainz, Germany, 1997
59. M. Ostrick, diploma thesis, University of Mainz, Germany, 1994
60. A. Natter, diploma thesis, University of Tübingen, Germany, 1995
61. D. Rohe, Ph.D. thesis, University of Mainz, Germany, 1998, publication in preparation
62. E. Quint, Ph.D. thesis, the University of Amsterdam, The Netherlands, 1988
63. E. Jans et al., Nucl. Phys. A **475**, 687 (1987)
64. R. Florizone, MIT, Cambridge, Massachusetts, USA (private communication)
65. C. Marchand, Ph.D. thesis, the Université de Paris–Sud (France), 1987
66. D. Drechsel, University of Mainz, Germany (private communication)
67. Ch. Elster, Ohio University, Ohio, USA (private communication)
68. J. Osborne, Ph.D. thesis, University of California, Davis, California, USA, 1995
69. J. Becker et al., in *Proc. of the Int. Workshop on Polarized Beams and Polarized Gas Targets*, Cologne, Germany, June 1995, World Scientific, p. 16
70. W. Heil, Proc. to the Int. Symposium on Weak and Elektromagnatic Interactions in Nuclei, Osaka, Japan, June 1995
71. J. Becker et al., in *Proc. to the 12th Int. Symposium on High–Energy Spin Physics*, Amsterdam, The Netherlands, Sept. 1996, World Scientific, p. 204
72. J. Becker et al., in *Proc. of the Int. Workshop on Polarized Gas Targets and Polarized Beams*, Urbana, Illinois, USA, Aug. 1997, AIP Conference Proceedings 421, p. 36
73. D. Eyl et al., Zeitschr. f. Physik, A **352**, 211 (1995)
74. H. Arenhövel et al., Zeitschr. f. Physik, A **331**, 123 (1988)
75. H. Arenhövel, University of Mainz, Germany (private communication)
76. J. Jourdan, Nucl. Phys. A **603**, 117 (1996)